Optimal Finite-Difference Sub-Gridding Techniques Applied to the Helmholtz Equation

John W. Nehrbass, *Member, IEEE*, and Robert Lee, *Member, IEEE*

***Abstract*—Since the spatial resolution of a uniform grid determines in part the accuracy of a given simulation, it must be judiciously chosen. In some small region of the computation domain, a fine grid density may be needed, while in the remainder of the domain, a coarser grid is acceptable. It would be preferable if a coarse resolution could be used over the majority of the computational domain, while locally using a finer resolution around the problem areas. In this presentation, a systematic method is presented that shows how to optimally choose the finite-difference coefficients for the transition region from a coarse to a fine grid. Results are presented for two-dimensional problems and for specific stencils. The ideas can then be applied to any dimension and any desired stencil in a straightforward manner. The sub-gridding methods are verified for accuracy through a study of scattering from curved geometries and propagation through dense penetrable materials.**

***Index Terms*—Electromagnetic analysis, finite-difference methods, modeling, numerical analysis.**

I. Introduction

THE finite-difference (FD) method is a powerful computational technique for modeling electromagnetic phenomena. It is both easy to implement and computationally efficient. One of the problems with FD methods is their inability to accurately handle different grid spacings. For many cases, there may exist small isolated regions with a finer resolution requirement than the rest of the problem space. These locations occur when there is a high material property contrast or when stairstepping is used to model nonorthogonal geometries. Researchers have developed nonuniform gridding techniques in which an interpolation scheme is used to perform the finite differencing (an example of such is demonstrated in [1] and [2]). In these methods, we can transition between one cell size and another by slowly increasing or decreasing the grid spacing in the transition region. Unfortunately, the nonuniform gridding concept has many problems. There is a loss in accuracy within the transition region, especially if the transition region is small. Also, the aspect ratio of some of the FD cells may become very large, which further degrades the accuracy of the solution. Due to all of these factors, researchers in recent years have been trying to develop sub-gridding methods in which FD cells of two different sizes directly join. Several researchers [3]–[7] have come up with algorithms for finite difference time domain (FDTD) to perform the subgridding based on the use of interpolation and extrapolation of the field values at the interface between the two grids of differing resolution.

In this paper, a systematic method is presented that shows how one may optimally choose the FD coefficients at the interface between the two grids to approximate the Helmholtz equation. These coefficients are chosen based on physical "*electromagnetic considerations*" and, therefore, are not optimal for any arbitrary function. The ideas for this sub-gridding scheme come from the work in [8]. The FD coefficients are optimized for plane waves propagating at an arbitrary angle through the grid. While this paper derives results for two-dimensional (2-D) problems and for specific stencils, the theory is general and can be applied to any dimension and any desired stencil in a straightforward manner. In order to provide further support for this theory, our sub-gridding method is compared to one in which standard linear interpolation/extrapolation is used. We show that our method maintains the second-order accuracy of the original FD method, while the method based on linear interpolation/extrapolation is only first-order accurate. Also, we consider its application to scattering from curved geometries and propagation through dense penetrable materials.

II. Subgridding Theory

In [8], the 2-D Helmholtz equation is approximated by the traditional five-point stencil on a uniform grid. The optimal FD coefficients are then found to minimize the phase error in the solution. Due to the reduction in phase error, the method in [8] is called the reduced dispersion FD method. For the subgridding method, we apply the same method, except to an arbitrary stencil. To determine the stencils of interest, the following meshing scheme is adopted. First, a coarse mesh is established and placed throughout the computational domain. Next, sensitive regions are defined where a finer resolution is desired. In these sensitive regions, the resolution is doubled so that every coarse cell in this region is now divided into four finer cells. We refer to the region in which adjacent cells do not have the same spatial resolution as the transition region. If still finer resolutions are required, the process is again repeated. By adopting this meshing scheme, all transition regions will contain adjacent cells with a $2:1$ ratio of resolutions. As illustrated in Fig. 1, one can pass from the most coarse mesh to a mesh 2^{tran} times as fine in the space of only one coarse cell. Here, tran represents the number of transitions that are required. This allows the user to grid to an arbitrarily fine resolution while retaining a course gridding in the majority of the problem domain . The only restriction is that the material properties within the transition region must be homogeneous.

Manuscript received September 11, 1998. This work was supported by the Joint Services Electronics Program under Contract N00014-89-J-1007.

J. W. Nehrbass is with the Ohio Supercomputer Center, The Ohio State University, ASC/HP Wright Patterson AFB 45433-7802 USA.

R. Lee is with the ElectroScience, Laboratory, Department of Electrical Engineering, The Ohio State University, Columbus, OH 43212 USA.

Publisher Item Identifier S 0018-9480(00)04660-3.

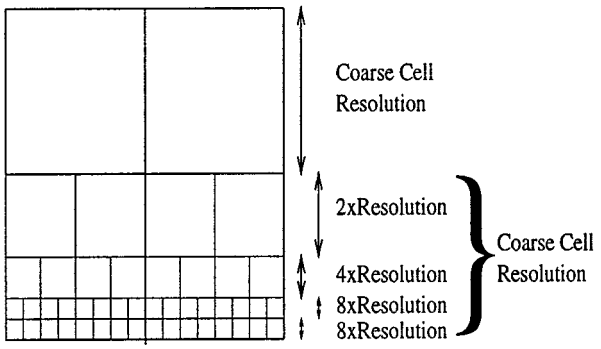

Fig. 1. Sampling location convention.

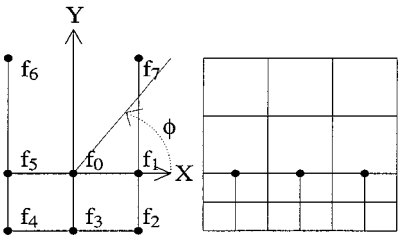

Fig. 2. Middle stencil.

Let us consider a function f, which satisfies the Helmholtz equation in a homogeneous region of space. There are three stencils used in the subgridding method to discretize the Helmholtz equation. These stencils are referred to as the middle stencil, the cross stencil, and the corner stencil. The function f is discretized into nodal values on each stencil (f_0 through f_N with N depending on the stencil of interest). In the next three subsections, the derivation of the FD equations are presented for these three stencils. The lengthy mathematics are included in the appendixes for the interested reader.

A. FD Equation for the Middle Stencil

The stencil for the middle node f_0 is shown in Fig. 2. The associated FD equation in its most general form is given by

$$\frac{w_0 f_0 + w_1 f_1 + w_2 f_2 + w_3 f_3 + w_4 f_4 + w_5 f_5 + w_6 f_6 + w_7 f_7}{h^2} = 0 \tag{1}$$

where h is the spacing for the smaller grid, and w_0 through w_7 are the unknown FD coefficients. The goal is to choose the coefficients such that (1) is true for all solutions to the Helmholtz equation; however, it is not possible to do so. In general, the solution to the Helmholtz equation satisfies

$$\frac{w_0 f_0 + w_1 f_1 + w_2 f_2 + w_3 f_3 + w_4 f_4 + w_5 f_5 + w_6 f_6 + w_7 f_7}{h^2} = \mathrm{Res}(\phi) \approx 0 \tag{2}$$

where Res is a residual term, which we want to be as close to zero as possible. To minimize Res, we use a subset of all possible solutions of the Helmholtz equation, more specifically, a plane wave that propagates along an arbitrary direction

$$f = e^{jk\left(x\ \cos(\phi) + y\ \sin(\phi)\right)} \tag{3}$$

where k is the wavenumber and ϕ is the angle of propagation. The values of the plane wave sampled at the nodal locations are given as

$$\begin{aligned}
f_0 &= 1 \\
f_1 &= e^{jkh\ \cos(\phi)} \\
f_5 &= e^{-jkh\ \cos(\phi)} \\
f_3 &= e^{-jkh\ \sin(\phi)} \\
f_2 &= e^{jkh\left(\cos(\phi) - \sin(\phi)\right)} \\
f_4 &= e^{-jkh\left(\cos(\phi) + \sin(\phi)\right)} \\
f_6 &= e^{jkh\left(-\cos(\phi) + 2\ \sin(\phi)\right)} \\
f_7 &= e^{jkh\left(\cos(\phi) + 2\ \sin(\phi)\right)}.
\end{aligned} \tag{4}$$

The above can be rigorously solved for a given propagation angle. However, for arbitrary scatterers, a spectrum of plane waves may be present. Assuming that all angles are equally probable, the approximation is solved in an average sense as follows:

$$\int_0^{2\pi} h^2\,\mathrm{Res}(\phi)\,d\phi = 0. \tag{5}$$

Performing the integration and solving for w_0 yields

$$\begin{aligned}
w_0 = -\Big[&(w_1 + w_3 + w_5)J_0(kh) + (w_2 + w_4)J_0(\sqrt{2}kh) \\
&+ (w_6 + w_7)J_0(\sqrt{5}kh)\Big].
\end{aligned} \tag{6}$$

Before solving for the other coefficients, the number of unknowns is further reduced by exploiting the symmetry of the problem. The relations ($w_1 = w_5$, $w_2 = w_4$, $w_6 = w_7$) must hold true in order that the wave does not have a preferred propagation direction. One of the coefficients is fixed so that the others are uniquely determined. We choose $w_1 = w_5 = 1$ so that our approximating equation becomes

$$\begin{aligned}
w_2 &\left[2e^{-jkh\ \sin(\phi)}\ \cos\left(kh\ \cos(\phi)\right) - 2J_0(\sqrt{2}kh)\right] \\
&+ w_3\left[e^{-jkh\ \sin(\phi)} - J_0(kh)\right] \\
&+ w_6\left[2e^{j2kh\ \sin(\phi)}\ \cos\left(kh\ \cos(\phi)\right) - 2J_0(\sqrt{5}kh)\right] \\
&= 2\left[J_0(kh) - \cos\left(kh\ \cos(\phi)\right)\right]
\end{aligned} \tag{7}$$

which is rewritten in the form

$$W_1 F_1 + W_2 F_2 + W_3 F_3 = R \tag{8}$$

where $w_2 = W_1$, $w_3 = W_2$, $w_6 = W_3$ and

$$\begin{aligned}
F_1 &= 2e^{-jkh\ \sin(\phi)}\ \cos\left(kh\ \cos(\phi)\right) - 2J_0(\sqrt{2}kh) \\
R &= 2\left[J_0(kh) - \cos\left(kh\ \cos(\phi)\right)\right] \\
F_3 &= 2e^{j2kh\ \sin(\phi)}\ \cos\left(kh\ \cos(\phi)\right) - 2J_0(\sqrt{5}kh) \\
F_2 &= e^{-jkh\ \sin(\phi)} - J_0(kh).
\end{aligned} \tag{9}$$

Appendix A shows the process for finding the optimal coefficient values for this reduced equation. These coefficients are a function of only one variable (kh) and are plotted versus kh in

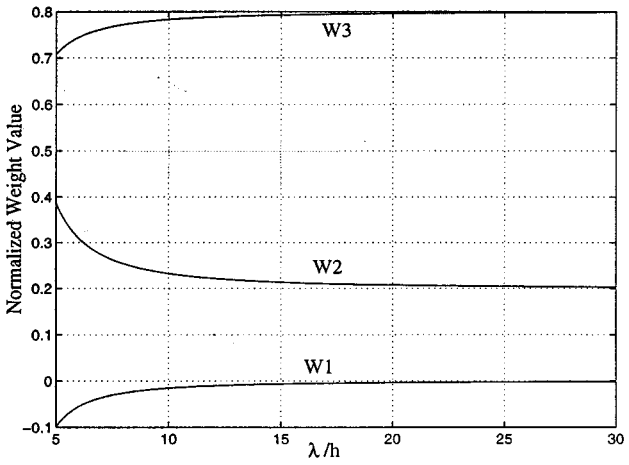

Fig. 3. Optimal coefficients for the middle stencil.

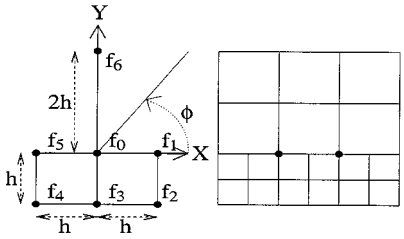

Fig. 4. Cross stencil.

Fig. 3. Note that the derivation of the coefficients for the cross and corner stencils are not given in this paper, but can be found in [9]. Greater accuracy can be achieved by coupling more nodes together; however, this decreases the sparsity of the resulting matrix. For the stencil selections presented, the given FD coefficients are the most optimal in the average sense.

B. FD Equation for the Cross Stencil

Next, the optimal interpolation scheme for the cross stencil is described. The values of the plane wave sampled at the nodal locations shown in Fig. 4 are given as

$$\begin{aligned} f_1 &= e^{jkh\,\cos(\phi)} \\ f_2 &= e^{jkh\left(\cos(\phi)-\sin(\phi)\right)} \\ f_3 &= e^{-jkh\,\sin(\phi)} \\ f_0 &= 1 \\ f_5 &= e^{-jkh\,\cos(\phi)} \\ f_4 &= e^{-jkh\left(\cos(\phi)+\sin(\phi)\right)} \\ f_6 &= e^{j2kh\,\sin(\phi)}. \end{aligned} \tag{10}$$

It is now desired to approximate the field in the center of the stencil f_0 as a function of the neighboring nodes

$$\frac{w_0 f_0 + w_1 f_1 + w_2 f_2 + w_3 f_3 + w_4 f_4 + w_5 f_5 + w_6 f_6}{h^2} = \mathrm{Res}(\phi) \approx 0. \tag{11}$$

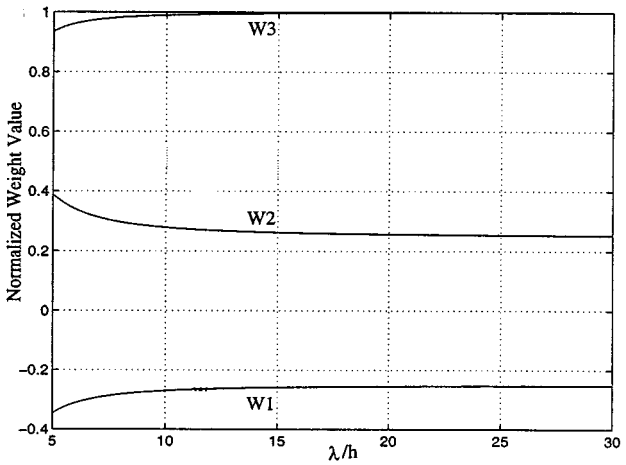

Fig. 5. Optimal coefficients for the cross stencil.

Proceeding as before, we integrate over 2π and solve for w_0 as

$$w_0 = -\Big[(2+w_3)J_0(kh) + 2w_2 J_0(\sqrt{2}kh) + w_6 J_0(2kh)\Big] \tag{12}$$

where we have made use of the symmetry and let $w_1 = w_5 = 1$, and $w_2 = w_4$. As before

$$W_1 F_1 + W_2 F_2 + W_3 F_3 = R \tag{13}$$

where $w_2 = W_1$, $w_3 = W_2$, $w_6 = W_3$ and

$$\begin{aligned} F_1 &= 2e^{-jkh\,\sin(\phi)}\,\cos(\cos\,\phi) - 2J_0(\sqrt{2}kh) \\ F_2 &= e^{-jkh\,\sin(\phi)} - J_0(kh) \\ F_3 &= e^{j2kh\,\sin(\phi)} - J_0(2kh) \\ R &= -2\Big[\cos\left(kh\,\cos(\phi)\right) - J_0(kh)\Big]. \end{aligned} \tag{14}$$

These optimal values are plotted versus kh in Fig. 5.

C. FD Equation for the Corner Stencil

Finally, the optimal FD equation for the corner interpolation nodes are derived. The values of the plane wave sampled at the nodal locations shown Fig. 6 are given as

$$\begin{aligned} f_1 &= e^{j\,2kh\,\cos(\phi)} \\ f_2 &= e^{-jkh\,\sin(\phi)} \\ f_3 &= e^{-j2kh\,\sin(\phi)} \\ f_7 &= e^{j\,2kh\,\sin(\phi)} \\ f_5 &= e^{-jkh\,\cos(\phi)} \\ f_6 &= e^{-j2kh\,\cos(\phi)} \\ f_4 &= e^{-jkh\left(\cos(\phi)+\sin(\phi)\right)} \\ f_0 &= 1. \end{aligned} \tag{15}$$

It is now desired to approximate the field in the center of the stencil f_0 as a function of the neighboring nodes

$$\frac{w_0 f_0 + w_1 f_1 + w_2 f_2 + w_3 f_3 + w_4 f_4 + w_5 f_5 + w_6 f_6 + w_7 f_7}{h^2} = \mathrm{Res}(\phi) \approx 0. \tag{16}$$

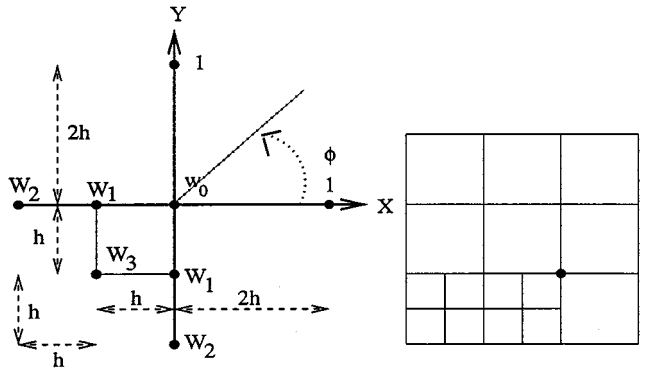

Fig. 6. Corner stencil.

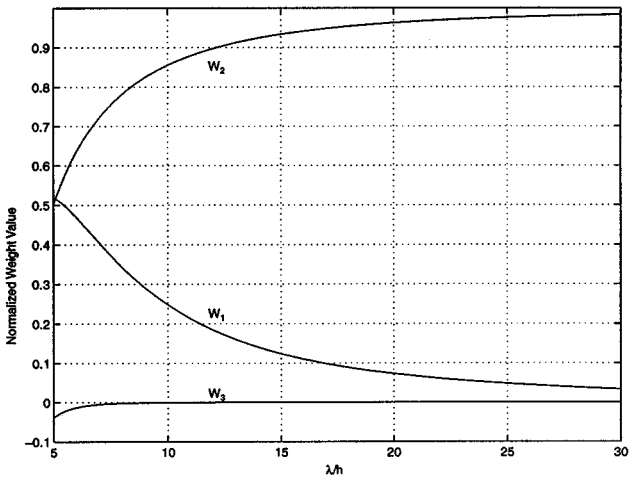

Fig. 7. Optimal coefficients for the corner stencil.

Again, we integrate over a 2π interval and solve for w_0 as

$$w_0 = -\Big[2(1+w_3)J_0(2kh) + 2w_2 J_0(kh) + w_4 J_0(\sqrt{2}kh)\Big] \tag{17}$$

where we have made use of the symmetry and let $w_1 = w_7 = 1$, $w_2 = w_5$, and $w_3 = w_6$. The simplified equation becomes

$$W_1 F_1 + W_2 F_2 + W_3 F_3 = R \tag{18}$$

where $w_2 = W_1$, $w_3 = W_2$, $w_4 = W_3$ and

$$\begin{aligned} F_1 &= e^{-jkh\,\sin(\phi)} + e^{-jkh\,\cos(\phi)} - 2J_0(kh) \\ F_2 &= e^{-j2kh\,\sin(\phi)} + e^{-j2kh\,\cos(\phi)} - 2J_0(2kh) \\ F_3 &= e^{-jkh\left(\cos(\phi)+\sin(\phi)\right)} - J_0(\sqrt{2}kh) \\ R &= 2J_0(2kh) - e^{j\,2kh\,\sin(\phi)} - e^{j\,2kh\,\cos(\phi)}. \end{aligned} \tag{19}$$

These optimal values are plotted versus kh in Fig. 7.

III. Numerical Verification

To study the accuracy of the proposed subgridding method, we consider several numerical experiments. The first is subgridding in free space, which allows us to obtain the order of accuracy of the subgridding scheme. The second numerical problem is scattering from a perfectly conducting circular cylinder, which demonstrates the ability of subgridding to accurately model nonorthogonal geometries. The last problem is plane-wave reflection from a dielectric interface of high-permittivity contrast. This problem shows the advantages of subgridding for such geometries.

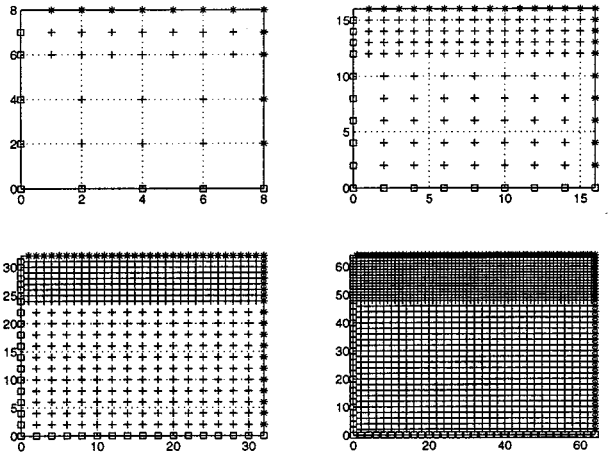

Fig. 8. Sample locations for different resolutions.

A. Free-Space Subgridding

To test out the errors due to subgridding, we consider a square computation domain of size $0.8\lambda \times 0.8\lambda$. Four different grids are considered for this region, as shown in Fig. 8. On the bottom and left-hand-side boundaries of this domain, we force Dirichlet boundary conditions, shown as squares in this figure. On the top and right-hand-side boundaries, we place a first-order absorbing boundary condition (ABC), depicted as stars. The upper portion of the domain contains a grid that is twice as fine as the lower portion. We choose the lower grid spacings to be $\lambda/10$, $\lambda/20$, $\lambda/40$, and $\lambda/80$ with sampling locations, shown as plus signs in Fig. 8.

The RDFD method (from [8]) is used for grid locations away from the transition region. For the nodes on the transition region, we calculated results by two different methods. First, the optimal equations, as described previously, are used. These results are compared to results obtained with simple linear interpolation in Fig. 9. The errors are shown for a plane wave propagating along angles from 0° to 90°. The solid curves are for linear interpolation cases where the largest error is for $h = \lambda/10$ and decreasing to the smallest error at $h = \lambda/80$. The star curves are the errors for the same grid densities with the new optimized method. Experiments show that one would have to use a grid spacing of $h = \lambda/53$ for the linear case in order to get the same level of error as that for the optimal case at $h = \lambda/10$. The order of each method as a function of wave propagation angle is shown in Fig. 10. These order of accuracy curves were produced from a least squares fit at each incidence angle of the error at the four grid densities shown in Fig. 8.

Using linear interpolation clearly reduces the accuracy from second to first order and appears to be a strong function of propagation angle. In contrast, the new method achieve almost second-order accuracy, while maintaining fairly constant results as a function of angle.

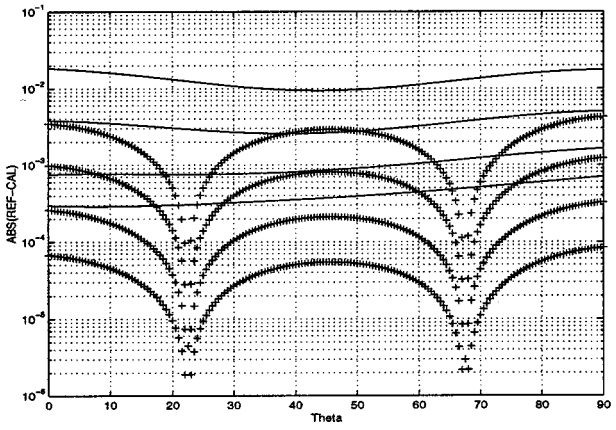

Fig. 9. Plot of the normalized error versus incidence angle of plane wave for both the optimized subgridding method (curves represented by $+$) and subgridding based on linear interpolation (curves represented by solid lines). The curves show the error for grid spacings of $\lambda/10$, $\lambda/20$, $\lambda/40$, and $\lambda/80$ where the error curves decrease with decreasing grid spacing.

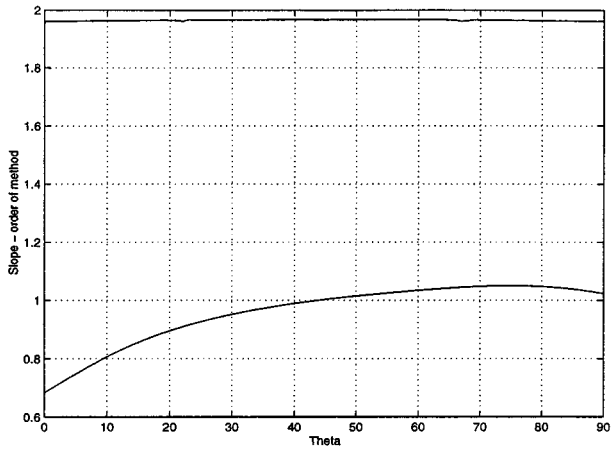

Fig. 10. Order of accuracy for the optimized subgridding method (curve near "2") versus subgridding based on linear interpolation (curve near "1").

B. Scattering from a PEC Cylinder

In this section, the sub-gridding methods are first numerically verified for accuracy through a study of the scattering from an infinitely long perfect electric conductor (PEC) circular cylinder excited by a plane wave. This geometry is chosen for a number of reasons. First, the solution of this problem is known in closed form. This allows us to compute the error in the predicted results. A desirable feature of the sub-gridding method is the ability to resolve curved surfaces. To this extent, the cylinder is a good choice.

We first model the scatterer by placing it in the center of a mesh consisting of 35 cells $\times$ 35 cells. The radius of the cylinder is chosen to be 4.5-cells wide. The spatial resolution for this example is fixed at $h = \lambda/15$. The reference solution for this problem is shown in Fig. 11. This solution is the exact solution as computed by an eigenfunction expansion. Here, the magnitude of the scattered field is plotted over the surface of the problem domain. From this figure, it is apparent where the energy has been reflected from the cylinder and where the cylinder shadows the incident wave.

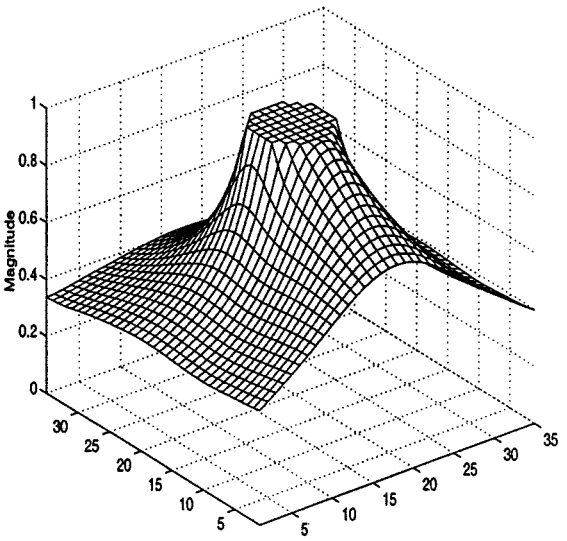

Fig. 11. Reference solution for plane wave scattering by a PEC cylinder.

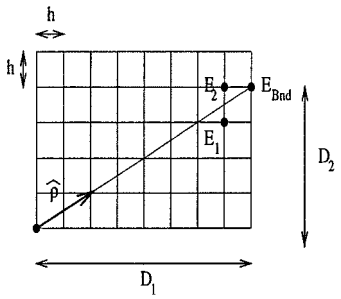

Fig. 12. Cylinder boundary conditions assuming a $\hat{\rho}$ propagating field.

For the calculated problem, we need to specify appropriate boundary conditions. It is assumed that as the energy is scattered from the cylinder, it propagates in a radially outward direction. From Fig. 12, we can approximate the field at the boundary (E_{Bnd}) as a weighted function of the fields only one cell inside the problem domain (E_1, E_2) times a phaser that propagates in the $\hat{\rho}$ direction

$$E_{\mathrm{Bnd}} = \left[\left(1 - \frac{D_2}{D_1}\right) E_2 + \frac{D_2}{D_1} E_1\right] e^{-jkh\sqrt{(D_2/D_1)^2+1}}. \tag{20}$$

The scattered field is calculated by using the four different sub-gridding meshes, as shown in Fig. 13. In the first case, we calculate the solution by using only the coarse mesh everywhere. The sampling locations are illustrated in Fig. 13 as plus signs. These are placed over every sampling location. For the remaining three meshes, a sensitive region around the cylinder is identified. This sensitive region occupies an area of 12 $\times$ 12 coarse cells with the cylinder located in the center. For the second, third, and fourth calculations, the meshes inside the sensitive region are resolved more finely in order to more accurately model the curvature of the cylinder. In the second calculation, the mesh size is half ($h = \lambda/30$) that of the first case. For the third case, the mesh is halved again ($h = \lambda/60$). In the fourth case, the mesh is halved ($h = \lambda/120$) yet again.

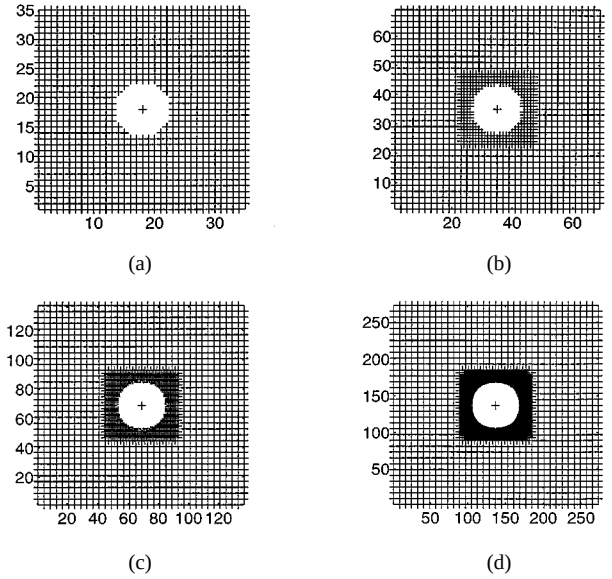

Fig. 13. Coarse and fine sampling locations indicated by "+" signs. (a) Coarse sample locations. (b) Coarse/2. (c) Coarse/4. (d) Coarse/8.

In the transition regions, the meshes follow the convention as explained earlier.

The results for these four cases are illustrated in Fig. 14. For these figures, the error is defined as the absolute value of the differences between calculated and exact values. This error is then plotted over the problem domain. Notice that in the first calculation (coarse mesh used everywhere), the largest error occurs directly behind the cylinder. This is the location where the cylinder shadows the incident wave. The maximum error has a relative value of 0.3086 and there are 1152 unknowns throughout the domain. In the second calculation, a rectangular region surrounding the cylinder is identified and given a spatial resolution twice as fine as in the coarse region. The maximum error for this calculation is reduced to 0.1684. Notice that the maximum error has been reduced by almost half, while the total amount of unknowns has only been increased to 1424. The maximum error generated in the third case was 0.1005 with 2164 unknowns used. For the fourth case, 4496 unknowns were used, generating a maximum error of 0.0835. As the mesh is further refined, the error continues to decrease, but not at such a dramatic rate. This error bound results from the region that maintains a coarse mesh. The error generated in the coarse region couples to the entire problem. When the contribution of error generated in the coarse region becomes more significant than the contribution of the error generated by approximating the curvature of the cylinder, global mesh refinement is required for further error reduction.

To exaggerate the usefulness of the sub-gridding technique, lets us reconsider the second case. If the same problem domain were to be examined using a uniform mesh size of $h = \lambda/30$, the number of unknowns required to calculate this region would be 4528. This implies that the sub-gridding technique allows one to calculate a problem of this sort with over a 3.9 times reduction in memory requirements. Matrix inversion is a $O(N^3)$ process; however, for this type of problem, the matrix is sparse. Depending on the bandwidth of the sparse matrix, the problem

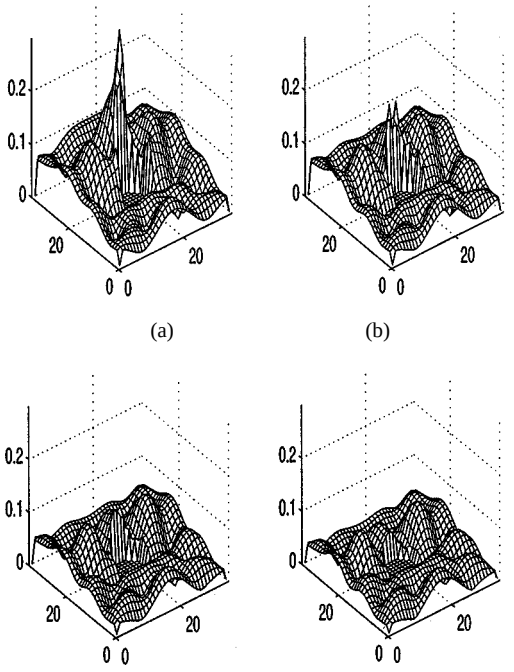

Fig. 14. Absolute value of the difference between the calculated and exact scattered field. (a) Coarse resolution. (b) Coarse/2. (c) Coarse/4. (d) Coarse/8.

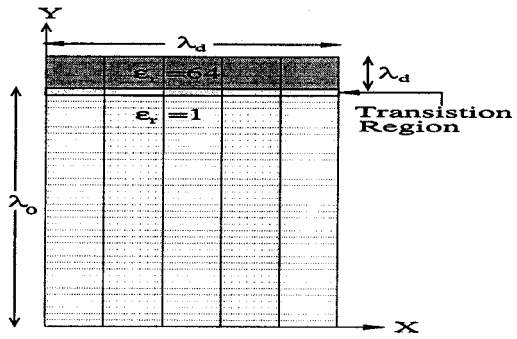

Fig. 15. Coarse grid placed over the semiinfinite dielectric half-plane ($\epsilon_r = 64$).

can be reduced as much as a $O(N^{1.5})$ process. This implies that the processing time will become somewhere between 8–59 times more efficient.

C. Wave Behavior Inside a Dense Dielectric Material

To add further support for the sub-gridding concept, energy propagating through a dense dielectric material is studied. For this case, we examine a semiinfinite dielectric half-space, as shown in Fig. 15. The dielectric has a relative dielectric constant of $\epsilon_r = 64$. The wavelength inside the dielectric (λ_d) is, therefore, one-eighth that of the free-space (λ_0) wavelength. A (λ_d) × (λ_d) region of the dielectric is sampled. The dimensions of the free-space region are one free-space wavelength (λ_0) by one dielectric wavelength (λ_d).

The coarse spatial resolution is chosen as a fortieth of a free-space wavelength ($h = \lambda_0/40$). While this sampling interval is sufficient to accurately model the field behavior in

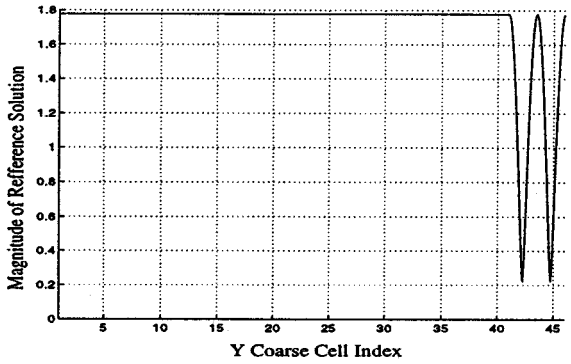

Fig. 16. Profile of the exact solution for the semiinfinite dielectric half-plane ($\epsilon_r = 64$).

the free-space region, it is not sufficient for the region inside the dielectric. Inside the dielectric, a sampling of $h = \lambda_0/40$ is equivalent to $h = \lambda_d/5$. The phase error generated by this coarse sampling will accumulate over the problem domain and produce unacceptable errors. For a plane wave traveling from within the dielectric incident normal to the dielectric free-space interface, the solution takes the profile shown in Fig. 16.

Notice that the magnitude of the reference solution goes through two oscillations as the dielectric is one-wavelength (λ_d) long. The sub-gridding method is used to sample this region at a more fine spatial resolution while maintaining a coarse resolution in the free-space region. Since the solution to this problem is known in closed form, Dirichlet boundary conditions are used at the truncation boundaries.

This problem is studied by using three different sub-gridding meshes of spatial resolutions: $h = \lambda_d/20$ (two transitions), $h = \lambda_d/40$ (three transitions), and $h = \lambda_d/80$ (4 transitions). The number of unknowns for these case are 574, 1818, and 6697, respectively. The errors, defined as the absolute value of the difference between exact and calculated results, for each case are illustrated in Fig. 17.

As evident from the provided illustrations, the sub-gridding works well, causing no abrupt discontinuous errors as the wave propagates through the transition region. Errors for all three cases are minimized near the boundaries and follow the same profile as the reference solution. Notice that if a spatial resolution of $\lambda_d/80$ were used everywhere, this would require 56 801 unknowns. Therefore, the sub-gridding method reduced the number of unknowns by over eight times, reduced the computation time by over 64 times, and maintained an acceptable error range. When results were calculated with a free-space coarse mesh used everywhere, the errors were so severe that they were not included in the illustrations. This sub-gridding method is, therefore, ideal for dense problems of this type.

IV. Summary

In this paper, a new subgridding method is presented that maintains the order of accuracy of the original FD method. A specific sub-gridding stencil is adopted for the 2-D examples in this paper; however, the theory is general enough so that other stencils and higher dimensions may be implemented. Results were verified by studying problems with known

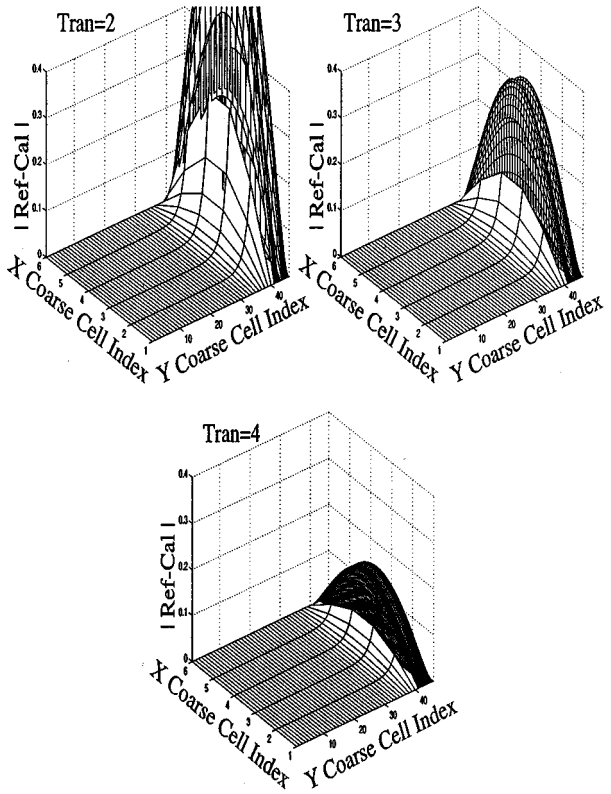

Fig. 17. Sub-gridding errors for the semiinfinite dielectric half-plane.

solutions. These sub-gridding techniques are shown to be useful when trying to increase accuracy while minimizing computational resources.

Appendix A
Optimization of the Coefficients

What values of W_i approximate $R(\phi)$ the best for all angles ϕ?

$$W_1F_1 + W_2F_2 + W_3F_3 \approx R. \tag{21}$$

This can be solved in a least squares sense by first defining an orthogonal basis P_i that spans the same space as the functions F_i. The inner product space for this system and the norm squared are, respectively, defined as

$$\langle F,\, P\rangle = \int_0^{2\pi} F(\phi)P^*(\phi)\,d\phi$$
$$\|F\|^2 = \langle F,\, F\rangle = \int_0^{2\pi} F(\phi)F^*(\phi)\,d\phi. \tag{22}$$

The Gram Schmidt Orthogonalization Process can be used to define an orthogonal basis P_i as

$$P_1 = F_1$$
$$P_2 = F_2 - \frac{\langle F_2,\, P_1\rangle}{\|P_1\|^2}P_1$$
$$P_3 = F_3 - \frac{\langle F_3,\, P_1\rangle}{\|P_1\|^2}P_1 - \frac{\langle F_3,\, P_2\rangle}{\|P_2\|^2}P_2. \tag{23}$$

Equation (21) can now be "best" approximated as

$$\frac{\langle R,\, P_1\rangle}{\|P_1\|^2}P_1+\frac{\langle R,\, P_2\rangle}{\|P_2\|^2}P_2+\frac{\langle R,\, P_3\rangle}{\|P_3\|^2}P_3\approx R. \tag{24}$$

Since F_i and P_i span the same space, the left-hand side of (21) can be equated to the left-hand side of (24). Now the values W_i can be approximated for by the least square method or exactly solved for. Since the least squared method is easily applied, the following section shows how one may execute the above-described process in order to solve for the various optimal middle stencil coefficients exactly. In order to reduce the length of the equations, the following list of variables are defined, and only the middle stencil coefficients are explicitly derived. Derivations for the cross and corner stencil coefficients are given in [9]

$$\begin{aligned}
J0 &= J_0(kh)\\
J2 &= J_0(2kh)\\
J3 &= J_0(3kh)\\
J4 &= J_0(4kh)\\
Js2 &= J_0\big(\sqrt{2}kh\big)\\
Js5 &= J_0\big(\sqrt{5}kh\big)\\
Js10 &= J_0\big(\sqrt{10}kh\big)\\
Js13 &= J_0\big(\sqrt{13}kh\big)\\
J2s2 &= J_0\big(2\sqrt{2}kh\big).
\end{aligned} \tag{25}$$

Appendix B
Coefficients for the Middle Stencil

The spanning set of functions for the middle stencil are

$$\begin{aligned}
F_1 &= 2e^{-jkh\,\sin(\phi)}\,\cos\big(kh\,\cos(\phi)\big)-2Js2\\
F_2 &= e^{-jkh\,\sin(\phi)}-J0\\
F_3 &= 2e^{j2kh\,\sin(\phi)}\,\cos\big(kh\,\cos(\phi)\big)-2Js5\\
R &= 2\Big[J0-\cos\big(kh\,\cos(\phi)\big)\Big].
\end{aligned} \tag{26}$$

An orthogonal set that spans the same space is

$$\begin{aligned}
P_1 &= F_1\\
P_2 &= e^{\left(-jkh\,\sin(\phi)\right)}\Big(d1+d2\,\cos\big(kh\,\cos(\phi)\big)\Big)+d3\\
P_3 &= d4\,\cos\big(kh\,\cos(\phi)\big)e^{\left(2jkh\,\sin(\phi)\right)}\\
&\quad+d5\,\cos\big(kh\,\cos(\phi)\big)e^{\left(-jkh\,\sin(\phi)\right)}\\
&\quad+d6e^{\left(-jkh\,\sin(\phi)\right)}+d7
\end{aligned} \tag{27}$$

where

$$\begin{aligned}
d1 &= 2Js2^2-1-J2\\
d2 &= 2J0(1-Js2)\\
d3 &= J0(1+J2-2Js2)\\
D1 &= \pi(4J3+4Js13-8Js5Js2)\\
D2 &= \pi\big(-8Js2^2+4(1+J2)\big)\\
D3 &= \pi(4d1Js10+2d2J3+2d2Js13-4Js5d1J0\\
&\quad-4Js5d2Js2)\\
D4 &= \pi\Big(2\big(d1^2+d3^2\big)+2J0\big(2d1d3+2d1d2\big)\\
&\quad+4d2d3Js2+d2^2(1+J2)\Big)\\
d4 &= 2D2D4\\
d5 &= -2D1D4-D2D3d2\\
d6 &= -D2D3d1\\
d7 &= -2D2D4Js5+2D1D4Js2-D2D3d3.
\end{aligned} \tag{28}$$

The coefficients are now defined as

$$\begin{aligned}
W_3 &= \frac{d4\langle R,\, P_3\rangle}{2\|P_3\|^2}\\
W_2 &= d1\left(\frac{\langle R,\, P_2\rangle}{\|P_2\|^2}+\frac{2W_3d6}{d1d4}\right)\\
W_1 &= \frac{\langle R,\, P_1\rangle}{\|P_1\|^2}+\frac{d2W_2}{2d1}-W_3\left(\frac{d2d6}{d1d4}-\frac{d5}{d4}\right).
\end{aligned} \tag{29}$$

Combining all of the above gives the closed-form solution for optimal coefficients in the middle stencil

$$\begin{aligned}
W_3 =& -\Big(J2s2+2J2Js5J0Js2-3J2s2J0^2\\
&-J2s2J0^2J2+4J2s2J0^2Js2-2J0^2Js5^2\\
&-2Js5J0Js10Js2+2Js5J0Js10+Js5Js13J0^2\\
&+J2s2J2-2J2s2Js2^2+Js5J3J0^2+4J0^2Js10\\
&-Js13J0^3-J3J0^3-Js5J3-Js5Js13\\
&+2Js5^2Js2-6J0^2Js10Js2+2J0^2Js10J2\\
&+2J0^3Js5+J2-3J0^2J2-J0^2J2^2-2Js2^2J2\\
&+J2^2+4Js5J0Js2-2Js5J0J2-J0J3\\
&+4J0J3Js2+4J0Js13Js2-J0Js13-2Js10Js2\\
&+4Js10Js2^3-2Js5J0-4Js2^2Js5J0\\
&-2Js2^2J0Js13-2Js2^2J0J3-2Js10J2Js2\\
&+4J0^2J2Js2)/(4J0^2Js5^2+4Js5J0Js10J2\\
&-8Js5J0Js10Js2+4Js5J0Js10-4Js5Js13J0^2\\
&-4Js5J3J0^2-2Js10^2J2-3J0^2+2J0^2J3Js13\\
&+4Js5Js2Js13+4Js5Js2J3-4Js10J0Js13Js2\\
&+2J2+4Js10J0J3-4Js10J0J3Js2\\
&+J0^2J3^2+J0^2Js13^2-2J3Js13+4Js10^2Js2^2\\
&+4Js10J0Js13-2Js5^2J2-Js13^2-2Js5^2-J3^2\\
&-4J0^2J2+4J0^2Js2-J0^2J2^2-2Js2^2J2+J2^2\\
&-2Js10^2-2Js2^2+1+4J0^2J2Js2\Big)
\end{aligned} \tag{30}$$

$$\begin{aligned}
W_2 =& 2\Big(-J2s2Js5J0+J2s2J0Js13Js2+Js10J2^2\\
&-J2s2Js5J0J2+2J2s2Js5J0Js2-2J2Js2\\
&+2Js2J3Js13+J2J0J3Js2+J2J0Js13Js2\\
&+J2Js5J0Js2-2J0^2Js5^2+2Js5^2Js2J2\\
&-2Js5J0Js10J2+2Js5J0Js10Js2\\
&-2Js5J0Js10+3Js5Js13J0^2-4Js5Js13Js2^2\\
&-4Js5J3Js2^2+3Js5J3J0^2+2Js5^2Js2+2J0^2\\
&-2J0^2J3Js13-Js2+2Js10J0Js13Js2
\end{aligned}$$

$$
\begin{aligned}
&-Js10J0J3+2Js10J0J3Js2-J0^2J3^2-2Js5^3J0\\
&-J0^2Js13^2-Js10J0Js13-2Js2^2Js10J2\\
&+3J0^2J2-3J0^2Js2+J0^2J2^2-Js5J3Js10\\
&-Js5Js13Js10+2Js5^2Js2Js10+2Js2^3\\
&-Js5J0Js2+Js2Js13^2+Js10J2+Js2J3^2\\
&+J2s2Js10-2J2s2Js10Js2^2-J2s2J0J3\\
&+J2s2Js10J2J2s2J0J3Js2+Js5J0\\
&-J2J0Js13-J2J0J3-Js5J0J2^2\\
&-J2s2J0Js13+Js5^2J3J0+Js5^2Js13J0\\
&+2Js2^3J2-J2^2Js2-3J0^2J2Js2)/(4J0^2Js5^2\\
&+4Js5J0Js10J2-8Js5J0Js10Js2\\
&+4Js5J0Js10-4Js5Js13J0^2-4Js5J3J0^2\\
&-2Js10^2J2-3J0^2+2J0^2J3Js13\\
&+4Js5Js2Js13+4Js5Js2J3-4Js10J0Js13Js2\\
&+2J2+4Js10J0J3-4Js10J0J3Js2\\
&+J0^2J3^2+J0^2Js13^2-2J3Js13+4Js10^2Js2^2\\
&+4Js10J0Js13-2Js5^2J2-Js13^2-2Js5^2\\
&-J3^2-4J0^2J2+4J0^2Js2-J0^2J2^2-2Js2^2J2\\
&+J2^2-2Js10^2-2Js2^2+1+4J0^2J2Js2\Big) \qquad (31)
\end{aligned}
$$

$$
\begin{aligned}
W_1 = -\Big(&-Js13J2-2J0Js5Js2J3-2J0Js5Js2Js13\\
&-J3J2+J0+4J0Js2Js5^2+4J0Js2Js10^2\\
&+J3J0^2J2+2Js5Js2J2+Js5-2Js10J0^2Js13\\
&+Js13J0^2J2-2Js10J0^2J3-2J0Js5^2+J0^3\\
&-2Js5^3-2J0Js10J2Js2-3Js5J0^2J2\\
&+2J0Js10J2-Js5J0^2-J2s2Js13-4J0Js2\\
&-J2s2J3-2J0Js10^2+4Js5^2J0Js10\\
&-2J2s2Js5J0^2+Js5J2+J2s2J0^2J3\\
&+J2s2J0^2Js13+2J2s2Js5Js2\\
&-2J0Js2J2s2Js10+2Js2^2J0+2Js10Js2Js13\\
&+J0^3J2-4J2J0Js2+2Js10Js2J3\\
&+2Js5J0Js13+2Js5J0J3-4Js10Js2^2Js5\\
&+2J2Js2^2J0-2Js5Js10^2+2J0J2s2Js10\\
&+J0J2)/(4J0^2Js5^2+4Js5J0Js10J2\\
&-8Js5J0Js10Js2+4Js5J0Js10\\
&-4Js5Js13J0^2-4Js5J3J0^2-2Js10^2J2\\
&-3J0^2+2J0^2J3Js13+4Js5Js2Js13\\
&+4Js5Js2J3-4Js10J0Js13Js2+2J2\\
&+4Js10J0J3-4Js10J0J3Js2+J0^2J3^2\\
&+J0^2Js13^2-2J3Js13+4Js10^2Js2^2\\
&+4Js10J0Js13-2Js5^2J2-Js13^2\\
&-2Js5^2-J3^2-4J0^2J2+4J0^2Js2-J0^2J2^2\\
&-2Js2^2J2+J2^2-2Js10^2-2Js2^2\\
&+1+4J0^2J2Js2\Big). \qquad (32)
\end{aligned}
$$

REFERENCES

[1] E. Kalnay De Rivas, "On the use of nonuniform grids in finite-difference equations," *J. Comput. Phys.*, vol. 10, pp. 202–210, 1972.

[2] S. Xiao and R. Vahldieck, "A fast FDTD analysis of guided wave structures using a continuously variable mesh with second order accuracy," *J. Int. Elect. Telecommun. Eng.*, vol. 41, pp. 3–14, Jan.–Feb. 1995.

[3] S. S. Zivanovic, K. S. Yee, and K. K. Mei, "A subgridding method for the time-domain finite-difference method to solve Maxwell's equations," *IEEE Trans. Microwave Theory Tech.*, vol. 39, pp. 471–479, Mar. 1991.

[4] D. T. Prescott and N. V. Shuley, "A method for incorporating different sized cells into the finite-difference time-domain analysis technique," *IEEE Microwave Guided Wave Lett.*, vol. 2, pp. 434–436, Nov. 1992.

[5] M. W. Chevalier, R. J. Luebbers, and V. P. Cable, "FDTD local grid with material traverse," *IEEE Trans. Antennas Propagat.*, vol. 45, pp. 411–421, Mar. 1997.

[6] M. Okoniewski, E. Okoniewski, and M. A. Stuchly, "Three-dimensional subgridding algorithm for FDTD," *IEEE Trans. Antennas Propagat.*, vol. 45, pp. 422–429, Mar. 1997.

[7] P. Monk, "Sub-gridding FDTD schemes," *ACES J.*, vol. 11, pp. 37–46, 1996.

[8] J. Nehrbass, J. Jevtic, and R. Lee, "Reducing the phase error for finite difference methods without increasing the order," *IEEE Trans. Antennas Propagat.*, vol. 46, pp. 1194–1201, Aug. 1998.

[9] J. W. Nehrbass, "Advances in finite difference methods for electromagnetic modeling," Ph.D. dissertation, Dept. Elect. Eng., Ohio State Univ., Columbus, OH, 1996.

John W. Nehrbass (S'91–M'97) was born in Buffalo, NY, in 1967. He received the B.S. degree in electrical engineering and the M.S. degree in electromagnetics from Arizona State University, Tempe, in 1989 and 1991, respectively, and the Ph.D. degree in electrical engineering from The Ohio State University, Columbus, in 1996.

He has been with the Aeronautical System Center (ASC) Major Shared Resource (MSRC), Wright-Patterson Air Force Base, OH, as part of the Department of Defenses (DoD) High Performance Computing Modernization Program since September 1996. He is employed through the Ohio Supercomputer Center and has been helping the DoD integrate electromagnetic algorithms to massively parallel platforms.

Dr. Nehrbass was nominated for the 1998 Computerworld Smithsonian Award. His work is archived in the National Museum of American History, Smithsonian Institution, Washington, DC.

Robert Lee (S'82–M'83) received the B.S.E.E. degree from Lehigh University in Bethlehem, PA, in 1983, and the M.S.E.E. and Ph.D. degrees from the University of Arizona, Tucson, in 1983 and 1990, respectively.

From 1983 to 1984, he was a Microwave Engineer with the Microwave Semiconductor Corporation, Somerset, NJ. From 1984 to 1986, he was a Member of the Technical Staff at Hughes Aircraft Company, Tucson, AZ. In addition, during the summers of 1987–1989, he was with Sandia National Laboratories, Albuquerque, NM. Since 1990, he has been with The Ohio State University, Columbus, where he is currently an Associate Professor. His major research interests are in the analysis and development of finite methods for electromagnetics.

Prof. Lee is a member of the International Union of Radio Science (URSI) and was a recipient of the 1996 URSI Young Scientist Award.